CrossMark

Soot Oxidation Activity of Redox and Non-Redox Metal Oxides Synthesised by EDTA–Citrate Method

Anjana P. Anantharaman[1] · Hari Prasad Dasari[1] · Jong-Ho Lee[2] · Harshini Dasari[3] ·
G. Uday Bhaskar Babu[4]

Abstract In the present study, redox (CeO_2, SnO_2, Pr_6O_{11} and Mn_3O_4) and non-redox (Gd_2O_3, La_2O_3 ZrO_2 and HfO_2) metal oxides were successfully synthesised using the EDTA–citrate complexing method and tested for soot oxidation activity. The characterization of the metal oxides is carried out using FTIR, XRD, BET surface area, pore volume analyser, SEM and TEM. The redox nature and metal–oxygen bond information of the metal oxides are obtained from XPS analysis. In redox metal oxides, three critical parameters [lattice oxygen binding energy, reduction temperature and Δr (ionic size difference of the corresponding metal oxide oxidation states)] govern the soot oxidation activity. Among the redox metal oxide samples, Mn_3O_4 and Pr_6O_{11} samples showed lower binding energy for oxygen (O_β—529.4, 528.9 eV respectively), lower reduction temperature (T_α—317 and 512 °C respectively) and have smaller Δr value (9 pm and 17 pm respectively). Thus, displayed a better soot oxidation activity (T_{50} = 484 and 482 °C respectively) than compared to other redox metal oxides. Among the non-redox metal oxides, HfO_2 sample displayed higher BET surface area (21.06 m^2/g), lattice strain (0.0157), smaller ionic radius (58.2 pm) and higher relative surface oxygen ratio (58%) and thus resulted in a significantly better soot oxidation activity (T_{50} = 483 °C) than compared to other non-redox metal oxides.

✉ Hari Prasad Dasari
energyhari@nitk.edu
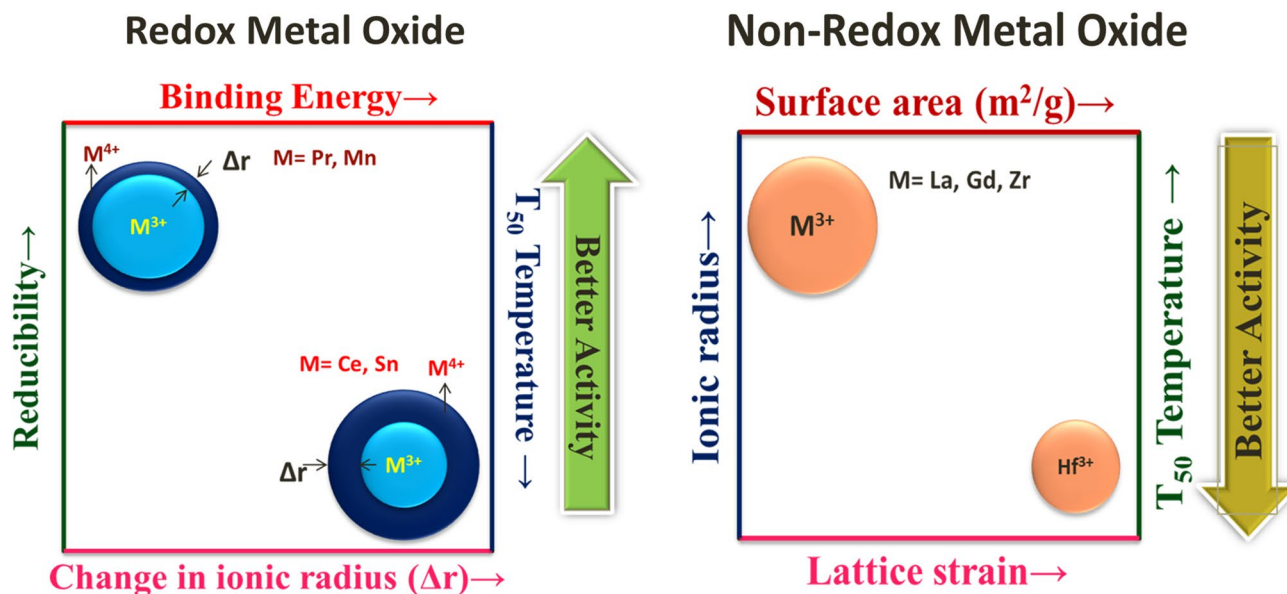
✉ Jong-Ho Lee
jongho@kist.re.kr

[1] Chemical Engineering Department, National Institute of Technology Karnataka, Mangalore 575025, India

[2] High-Temperature Energy Materials Research Center, Korea Institute of Science and Technology, Hwarangno 14-gil 5, Seongbuk-gu, Seoul 136-791, South Korea

[3] Chemical Engineering Department, Manipal Institute of Technology, Manipal 576104, India

[4] Chemical Engineering Department, National Institute of Technology Warangal, Warangal 506004, India

Graphical Abstract

Redox Metal Oxide

Binding Energy→

M^{4+} Δr M= Pr, Mn

M^{3+}

M= Ce, Sn M^{4+}

Δr M^{3+}

Reducibility→

Change in ionic radius (Δr)→

T$_{50}$ Temperature ↓

Better Activity

Non-Redox Metal Oxide

Surface area (m²/g)→

M= La, Gd, Zr

M^{3+}

Hf^{3+}

Ionic radius→

Lattice strain→

T$_{50}$ Temperature ↑

Better Activity

1 Introduction

Materialistic designing of soot oxidation catalyst must facilitate active oxygen species transfer from the catalyst to soot surface over a wide temperature range [1]. The basic information about oxygen vacancy formation, the number of defects and oxygen diffusion are necessary to understand the catalyst behaviour [2]. A catalyst with multiple oxidation state undergoes cyclic reduction and oxidation reaction which leads to continuous oxygen rich and lean condition, generally termed as Oxygen Storage Capacity (OSC) or Redox behaviour. Smooth delivery of lattice oxygen from catalyst surface to soot during the oxidation reaction and thus surface reducibility controls the activity [3, 4]. Active surface area availability, smaller crystallite size, smaller cell volume, effective cation radius, metal–oxygen interaction, soot and catalyst contact points and structural features are prominent specifications that favour surface oxygen availability and thus improve redox activity of catalyst [1, 5]. Acid surface sites available on the catalyst enhances active sites for adsorption on the catalyst surface and oxygen diffusion to the surface, which enables transfer of surface adsorbed oxygen to soot surface [1].

Oxygen buffering ability of ceria (CeO$_2$) plays a critical role in its catalytic applications apart from other important properties such as redox couple (Ce$^{3+/4+}$) [5], thermal stability [6], intermetallic M–Ce compounds formation

[5]. Increasing structural defect on CeO$_2$ enhances oxygen mobility and the number of oxygen vacancies which promote OSC and thus its activity [6]. Tin oxide (SnO$_2$) has rapid, reversible and interconvertible oxidation state between Sn^{2+}/Sn^{4+} even at a low temperature of around 200 °C, that are widely in use as catalyst support or promoter. Features such as surface oxygen deficiency and lattice oxygen species of SnO$_2$ promote its usage as oxidation catalyst especially for soot oxidation [7, 8]. The multivalent praseodymium cation (Pr^{3+}/Pr^{4+}) increases the redox potential of praseodymium oxide (Pr$_6$O$_{11}$) due to the high mobility of anion vacancy. The high reactivity of reduced species helps in active oxygen formation in catalyst surface with redox sites [9]. Manganese oxide (MnO$_x$) can exist in different oxidation state aids, in forming stable and defect oxides that benefit in a variety of catalytic properties [10]. Strong relation with particle size on activity is evident from catalytic performance of crystalline Mn$_3$O$_4$ and MnO$_2$ as per the study of Wagloehner et al. [1].

As observed by Christensen et al. [11], metal–oxygen bond strength is a key factor that affects the catalytic activity during soot oxidation. Their study with the heat of chemisorption proved that Co$_3$O$_4$ and CeO$_2$ showed optimum bond strength when compared to other transition metal oxides. Krishna et al. [12] studies single rare earth metal oxides (Sm, La, Pr, Y) and binary oxides of these rare earth metals doped with ceria. According to their work, non-redox metal oxides (Sm and La) have higher activity when compared to redox metal oxide (Pr) due to peroxide formation which is the free oxygen easily available to take part in soot oxidation reactions [12]. Soot oxidation study by John et al. [13] using different single metal oxides ranging from alkali,

alkaline, transition, rare earth metals and so on helps us to conclude that along with contact mode; material properties can also affect the activity of metal oxides. The activity of these metal oxides, when compared to CeO_2 is far better, may be due to the ready oxygen mobility of the materials [13]. The above mentioned reports [11–13] evidence that it is difficult to compare the results obtained from redox and non-redox materials since they differ in synthesis, processing and heat-treatment methods.

It is worth to mention that, synthesis, processing and heat-treatment conditions of these redox and non-redox metal oxides under similar conditions will lead to a better understanding of soot oxidation activity and the factors effecting it. From the literature [14, 15], it is evident that changes in synthesis, processing and heat-treatment conditions along with modification of cation material leads to changes in crystallite size, surface area, textural modifications, redox and active sites lead to affect the catalytic activity. To overcome this issue, in the present study, EDTA–citrate method is used to synthesize the redox and non-redox metal oxides and heat-treated at 600 °C for 5 h. EDTA–citrate method is chosen over various synthesis methods like Pechini gel technique [16], solid-state reaction [17], glycine nitrate process [18], microwave process [19] due to its uniqueness to obtain nano-scaled particle size and nice compositional homogeneity at molecular level during the synthesis process. In this approach metal complexes are formed by metal ion chelation, under high temperature, the chelates undergo polyesterification reaction and result in the plyometric glass with homogeneous metal ions [20]. Different metal oxides with redox (CeO_2, SnO_2, Pr_6O_{11} and Mn_3O_4) and non-redox (Gd_2O_3, La_2O_3 ZrO_2 and HfO_2) properties are synthesised. For the characterization of these metal oxides different techniques such as: Fourier Transform Infra-Red Spectroscopy (FT-IR), X-ray Diffraction (XRD), Brunauer–Emmett–Teller (BET) surface area, pore volume analyser, Scanning Electron Microscopy (SEM), Transmission Electron Microscopy (TEM) and X-ray Photon Spectroscopy (XPS) are used. The synthesised metal oxides are tested for soot oxidation under standard reaction condition.

2 Experimental Details

2.1 Materials

All the chemicals that are utilised for the synthesis of the catalyst were of AR grade. The metal nitrates such as Cerium nitrate hexahydrate [$Ce(NO_3)_3 \cdot 6H_2O$] ≥99% (SRL chemicals), Stannous chloride dihydrate ($SnCl_2 \cdot 2H_2O$) 98% (Loba), praseodymium nitrate hexahydrate [$Pr(NO_3)_3 \cdot 6H_2O$] 99.9% (Sigma), gadolinium nitrate hexahydrate [$Gd(NO_3)_3 \cdot 6H_2O$] 99.9% (Sigma), lanthanum

nitrate hexahydrate [$La(NO_3)_3 \cdot 6H_2O$] 99% (Sigma) zirconyl nitrate hydrate [$ZrO(NO_3)_2 \cdot 6H_2O$] 99.5% (Acros), hafnium chloride ($HfCl_4$) (Aldrich) and manganese nitrate hydrate 98% [$Mn(NO_3)_2 \cdot xH_2O$] (Sigma) are used as precursor salts to synthesise the respective single metal oxide solid solutions. Ammonium hydroxide solution NH_4OH (25% ammonia) (spectrum reagents) is used to adjust the pH to the basic condition. Ethylene diamine tetra acetic acid (EDTA) ≥99% (SRL chemicals) and citric acid monohydrate ≥99% (SRL chemicals) are used as chelating agents. EDTA–citrate complexing method [20] is used to synthesise the single metal oxide catalysts. The obtained solid black precursor after the oven drying at 150 °C/24 h is calcined at 600 °C/5 h to get the corresponding metal oxide sample. CeO_2, SnO_2, Pr_6O_{11}, Gd_2O_3, La_2O_3 ZrO_2, HfO_2 and Mn_3O_4 single metal oxides were successfully synthesised using the EDTA–citrate complexing method.

2.2 Characterization of Metal Oxide Catalyst

FTIR analysis is done in Bruker (Alpha) KBr/ATR in the range of 375–7500 cm^{-1} with KBr Optics and high sensitivity DLATGS. Using XRD technique, structural features of the metal oxide solid solutions were studied. XRD patterns were recorded on a XPERT Pro diffractometer using Cu Kα (0.1540 nm), operated at 40 kV and 30 mA in the 2θ range of 20°–80° with a step size of 0.02 and a time for the step is 2 s. The average crystallite size and the lattice parameter of the solid solutions were estimated using full width half maximum (FWHM) of the most prominent XRD peak using Debye–Scherer equation. The BET surface area and pore volume of the samples are measured using (SMARTSORB-92/93) instrument. Before the analysis, the samples were evacuated at 150 °C for 3 h to remove the residual moisture and flushed with nitrogen gas for 2 h. SEM (JSM-6380LA) and TEM (Jeol/JEM 2100) were used for the microstructural analysis such as shape and morphology of the obtained powders and its agglomerates. XPS analysis was performed in ultra-high vacuum using an (Omicron ESCA+) with a background pressure (6.7×10^{-8} Pa) and monochromator Al Kα (1486.6 eV) anode (25W, 15 kV). The spot size was 100×100 μm and the recorded spectra were calibrated by the standard binding energy (BE) peak at 284.6 eV belonging to the contaminant carbon in 1 s region.

2.3 Activity Measurement

Soot oxidation reaction using different metal oxides as a catalyst is conducted in a TG/DTA 6300 TGA instrument operating at a temperature range of 200–800 °C with a heating rate of 10 °C/min using air as a purge gas at a flow rate of 100 ml/min. The reaction is conducted under tight contact condition with a soot:catalyst ratio of 1:4 ground in mortar

and pestle for 30 min. Samples are preheated at around 100 °C to remove moisture content bound on their surface.

3 Results and Discussion

3.1 Fourier Transform Infra-Red (FT-IR) Spectroscopy

FTIR analysis of the metal oxides was carried out to investigate the metal-oxide bond formation in the respective metal oxides and also to find out the presence of impurities in the metal oxides. Figure 1 depicts the FTIR spectrum in the range of 1000–400 cm^{-1} for the single metal oxides synthesised by the EDTA–citrate complexing method and calcined at 600 °C/5 h. All the single metal oxide samples displayed metal–oxygen bond in the range of 700–350 cm^{-1}. For CeO$_2$ sample, a sharp, intense peak at 478 cm^{-1} represent the transverse mode of cubic fluorite structure and 2 weak intense peaks at 446 and 436 cm^{-1} represents the longitudinal mode of Ce–O stretching [21]. SnO$_2$ sample displayed one sharp peak at 623 cm^{-1} and 1 weak peak at 473 cm^{-1} and these peaks correspond to the O–Sn antisymmetric stretching mode of surface bound oxide and tetragonal O–Sn stretching vibration [21]. For Pr$_6$O$_{11}$ sample, the
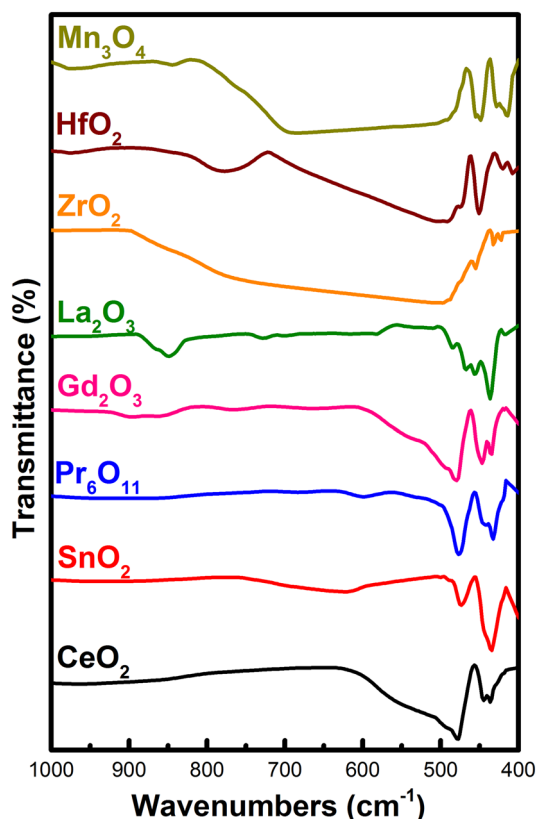
peak at 599 cm^{-1} confirms the Pr–O bond and a sharp peak at 476 cm^{-1} is the characteristic peak of Pr$_6$O$_{11}$ phase [21]. The peaks at 479 cm^{-1} correspond to bending of Gd–O for Gd$_2$O$_3$ [22] and La$_2$O$_3$ indicates a peak at 436 cm^{-1} confirms the vibration of La–O in the sample [23]. ZrO$_2$ sample shows two adjacent peaks at 432 and 423 cm^{-1} represents the symmetric Zr–O stretching mode of ZrO$_2$ with tetragonal phase [24]. Broad peak around 777 and 492 cm^{-1} and a sharp peak at 451 cm^{-1} are evident from HfO$_2$ sample which is mainly due to stretch vibration of Hf–O in bulk HfO$_2$ sample [21]. 449 cm^{-1} peak of Mn$_3$O$_4$ indicates the Mn–O stretching vibration [21]. From the result, we can see that the samples do not have any sign of impurity formation after calcination step. Thus, from FTIR analysis of the single metal oxide samples, it can be observed that the samples synthesised showed metal-oxide bonds and the peaks are matched well with the literature [21–24]. Further, XRD analysis is carried out to find out the nature of the phase, crystallite size and further identify the presence of any other impurities that cannot be detected by FTIR analysis.

3.2 X-ray Diffraction (XRD)

Figure 2 demonstrates the XRD patterns of the calcined single metal oxides. From the XRD patterns of CeO$_2$ and SnO$_2$ samples, all the major peaks related to cubic fluorite structure [25] and tetragonal structure [26] are noticeable, respectively. Pr$_6$O$_{11}$ and Gd$_2$O$_3$ samples revealed all the major peaks that are related to cubic fluorite structure [27, 28]. On the other hand, La$_2$O$_3$ sample showed a hexagonal structure [with (101) and (012) planes] along with some impurity in monoclinic phase corresponding to lanthanum oxycarbonate (La$_2$O$_2$CO$_3$). One of the reasons for the
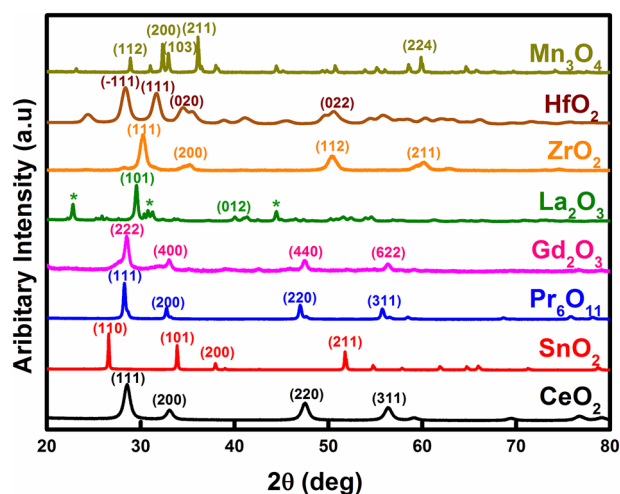

Fig. 1 FT-IR spectra of CeO$_2$, SnO$_2$, Pr$_6$O$_{11}$, Gd$_2$O$_3$, La$_2$O$_3$, ZrO$_2$, HfO$_2$ and Mn$_3$O$_4$ single oxides calcined at 600 °C/5 h

Fig. 2 XRD pattern of CeO$_2$, SnO$_2$, Pr$_6$O$_{11}$, Gd$_2$O$_3$, La$_2$O$_3$, ZrO$_2$, HfO$_2$ and Mn$_3$O$_4$ samples calcined at 600 °C/5 h. *Asterisk* indicates La$_2$O$_2$CO$_3$

formation of an impurity phase might be due to continuous exposure of the sample in air atmosphere since La_2O_3 sample is highly unstable in an air atmosphere and can easily adsorb CO_2 and transform into an impurity phase [13, 29]. ZrO_2 sample displayed peaks corresponding to the tetragonal structure from XRD plot [30]. Similarly, HfO_2 shows their characteristic peaks corresponding to monoclinic structure [31] and Mn_3O_4 corresponds to tetragonal structure [32]. Except for La_2O_3 sample, all the other samples demonstrated corresponding metal oxides and didn't contain any impurities. The impurity presence in La_2O_3 may affect its activity since the active sites availability due to impurity presence can act as intermediate and thus aid or suppress the activity. Table 1 shows the physical properties of the metal oxides related to phases, the lattice constant (a) (Å), crystallite size (D) (nm), BET surface area (m^2/g), Pore volume, Particle size (nm) calculated from BET Surface area, Lattice strain (ε) and Degree of agglomeration (ϕ). For the metal oxides, the crystallite size is in the range of 9–56 nm in which HfO_2 sample showed lowest crystallite size (~9 nm) and SnO_2 showed highest crystallite size (~56 nm). CeO_2 sample showed the highest surface area (~41 m^2/g) and SnO_2 sample showed the lowest surface area (0.7 m^2/g). The surface area of all other samples lies within this range. Pore volume lies in the range of 0.0006–0.0552 cm^3/g, lowest for SnO_2 and highest for Gd_2O_3. The particle size calculated from BET surface area of samples lies in the range of 1107–19 nm with SnO_2 having the largest and CeO_2 with the lowest value. The particle size of all other samples lies within this range. The particle size calculated from the BET surface area is larger than the crystallite size calculated from the XRD peaks. This reflects that the particles are agglomerated and the degree of agglomeration (ϕ) (ratio of crystallite size obtained from XRD and the particle size obtained from BET surface area) is in the range of 0.027–0.615 and it indicates that all the

samples are agglomerated. The lowest and highest degree of agglomeration is obtained for CeO_2 and La_2O_3 samples, respectively. The degree of agglomeration of all the other samples lies within the range.

The effect of crystallite size and surface area on the soot oxidation activity of these metal oxides will be discussed later. In general, as the surface area increases the active sites for the catalytic activity also increases thus showing an enhancement in the catalytic efficiency [33]. This statement may not hold good for all the catalytic reactions, in some cases like soot oxidation, the surface area may or may not be the key factor that affects the catalytic activity. Thus it is important to understand the fundamental properties of the oxides which profoundly influences the soot oxidation conversion [34]. The metal oxides synthesised have a broad range of surface area which can be due to specific surface nature. Pore volumes of our sample are relatively low compared to other work [12]. SEM and TEM analysis has been used to further analyse the morphology on different metal oxides and its effect on soot activity.

3.3 SEM and TEM Analysis

SEM analysis is carried to understand the structural morphology of these metal oxides. Figure 3 illustrates the morphology of CeO_2, SnO_2, Pr_6O_{11}, ZrO_2, HfO_2 and Mn_3O_4 samples. From Fig. 3a, it can be observed that the CeO_2 sample has flaky nature agglomerates [35] and whereas from Fig. 3b SnO_2 sample displayed individual or elongated octahedron type of agglomerates [36]. Figure 3c for praseodymium oxide (Pr_6O_{11}) have ovoid agglomerates with spherical particles [37]. The ZrO_2 SEM micrograph from Fig. 3d has a plate-like agglomerate structure [38]. From Fig. 3e, f, HfO_2 [38], Mn_3O_4 [39] samples displayed plate-like and spherical agglomerate structures, respectively.

Table 1 Lattice phases, crystallite size and surface area of single metal oxides calcined at 600 °C/5 h

Metal oxide	Phase	Lattice constant (Å)	Crystallite size (nm)	BET surface area (m^2/g)	Pore volume (cm^3/g)	Particle size (nm)	Lattice strain (ε)	Degree of agglomeration (ϕ)
CeO_2	Cubic	a = 5.4	11.7	41.2	0.0545	19	0.0125	0.61
SnO_2	Tetragonal	a = b = 4.7 c = 3.2	55.9	0.8	0.0006	1107	0.0028	0.05
Pr_6O_{11}	Cubic	a = 5.5	28.5	3.6	0.0059	221	0.0052	0.13
Gd_2O_3	Cubic	a = 10.8	16.3	4.6	0.0552	177	0.0092	0.09
La_2O_3	Hexagonal	a = b = 4.1 c = 5.8	29.9	0.9	0.0033	1084	0.0054	0.03
ZrO_2	Tetragonal	a = b = 5.1 c = 5.2	12.3	7.2	0.0245	147	0.0112	0.08
HfO_2	Monoclinic	a = 5.1 b = 5.2 c = 5.2 β = 99.1	9.4	21.1	0.0392	29	0.0157	0.32
Mn_3O_4	Tetragonal	a = b = 5.5 c = 10.1	46.9	1.8	0.0067	652	0.0025	0.07
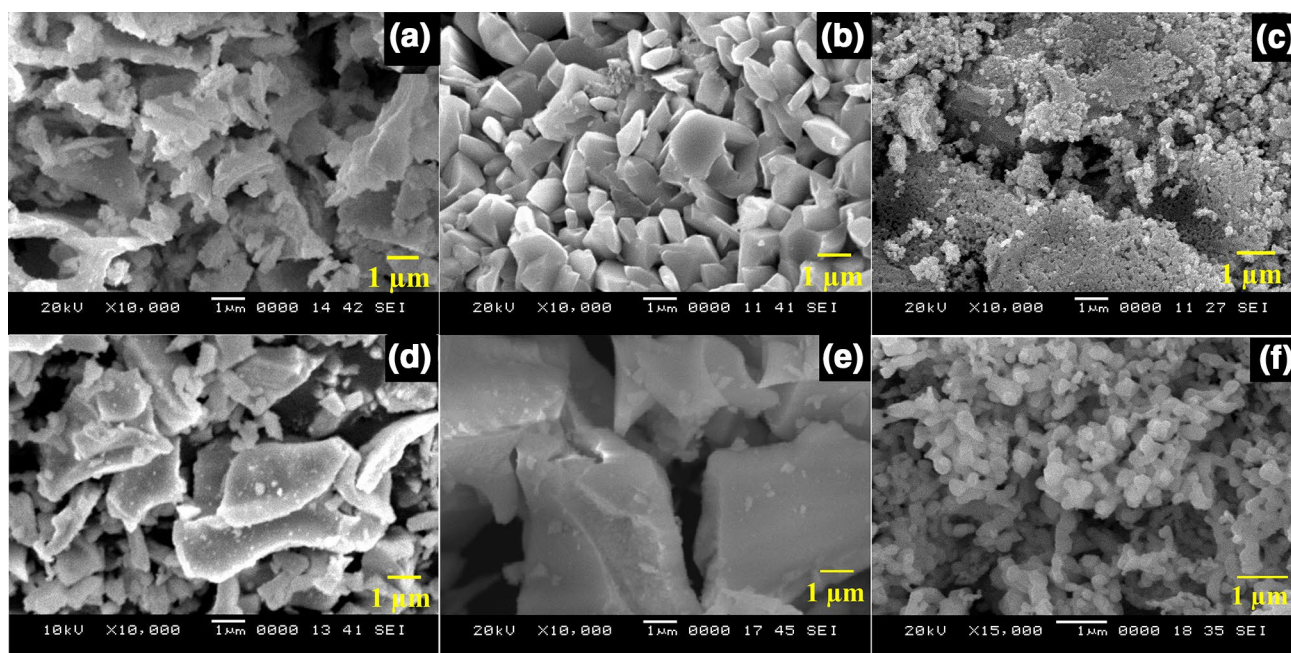
Fig. 3 SEM micrographs of **a** CeO_2, **b** SnO_2, **c** Pr_6O_{11}, **d** ZrO_2, **e** HfO_2 and **f** Mn_3O_4 samples calcined at 600 °C/5 h

Figure 4a, b depicts the TEM images of CeO_2 sample. The nano-particle size is within the range of 6–11 nm. The interplanar distance obtained from HR-TEM image (Fig. 4b) is 3.13 Å and it corresponds to (111) plane of CeO_2 sample. The average particle size is ~11 nm which matches well with crystallite size (~11 nm) obtained from XRD analysis of CeO_2 sample. Figure 4c depicts the SAED pattern in which each ring corresponds to each plane and their interplanar distance matches with the corresponding planes in XRD results [40]. Figure 5a–c demonstrates the TEM images and SAED patterns of La_2O_3 sample. From Fig. 5a, b, it is very hard to identify the nano-particle nature and from XRD patterns (Fig. 2) of La_2O_3 sample it hints that the impurity phase

($La_2O_2CO_3$) dominates the morphology (Fig. 5a, b) of La_2O_3 sample. The SAED patterns (Fig. 5c) clearly shows the dotted rings instead of line rings which confirms the presence of multiple phases in the La_2O_3 sample and this corroborates with the XRD results.

3.4 XPS Analysis

3.4.1 Redox Metal Oxides

The surface elemental analysis and oxidation state can be identified effectively using XPS analysis [41]. The redox samples (CeO_2, SnO_2, Pr_6O_{11} and Mn_3O_4) are analysed by
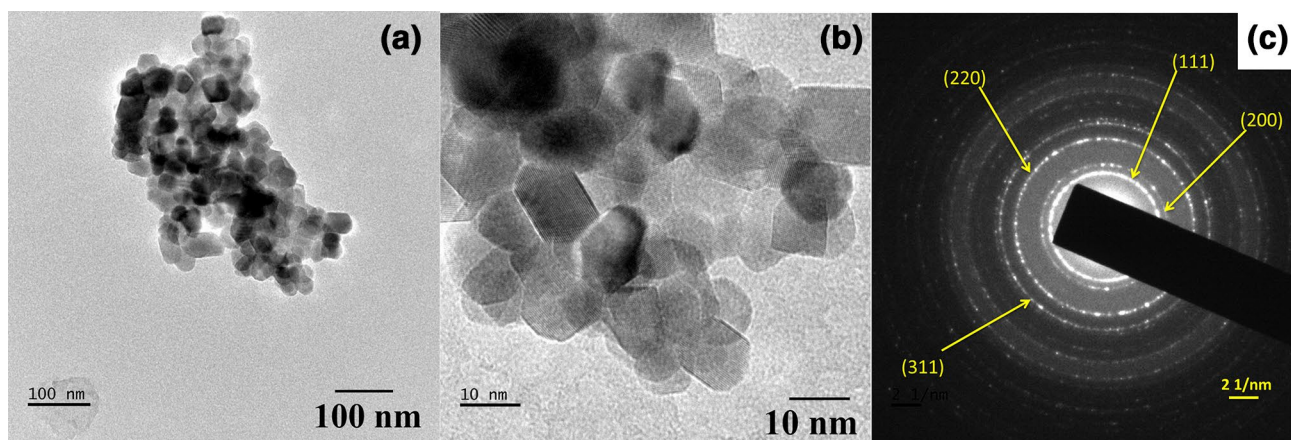

Fig. 4 **a, b** TEM image of CeO_2 and **c** SAED pattern of CeO_2 sample
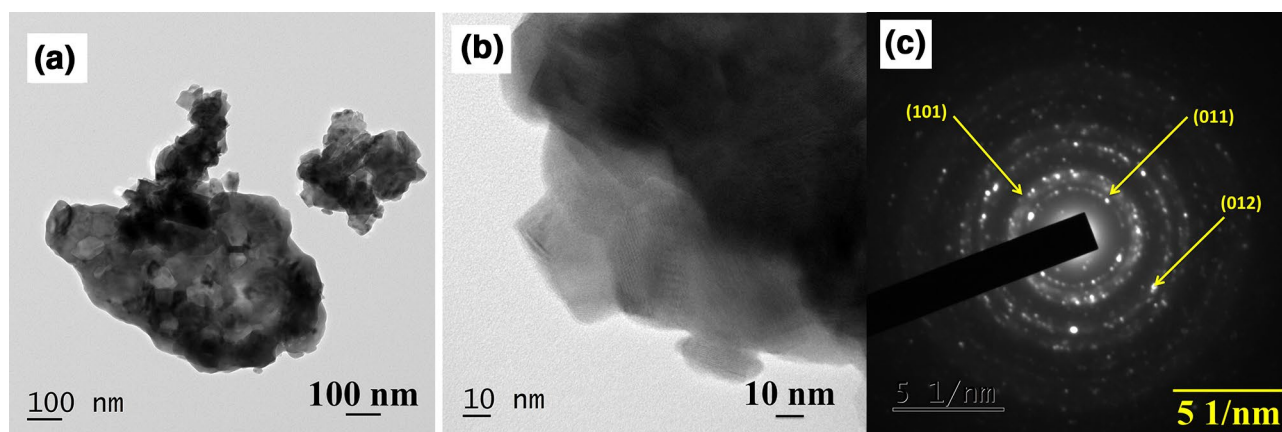
Fig. 5 **a, b** TEM image of La_2O_3 and **c** SAED pattern of La_2O_3 sample

XPS analysis to determine the multiple oxidation states and O1s bonding. Figures 6 and 7 shows results of Ce 3d, Sn 3d, Pr 3d and Mn 2p and O1s bonds of CeO_2, SnO_2, Pr_6O_{11}, and Mn_3O_4, respectively. All the peaks are fitted using Gaussian profiles and C corrected. Ce 3d peak in Fig. 6a shows a broad range of spectrum confirming multiple oxidations states. Designation of $3d_{3/2}$ and $3d_{5/2}$ indicates two sets of spin-orbital contributions that are represented in the figure as u and v respectively. The peaks shown as u′, u, v″, v′, v corresponds to Ce^{4+} oxidation state and u_0, v_0 corresponds to Ce^{3+} oxidation states [41]. These peaks confirm the presence of multiple oxidation states of Ce [24]. Peaks in Fig. 6b depicts the XPS peaks of SnO_2 sample and the peaks corresponding to $3d_{3/2}$ and $3d_{5/2}$ at 495 and 486 eV respectively represent Sn^{4+} oxidation state and shoulder peaks at 494 and 485 eV corresponds to Sn^{2+} oxidation state [7]. Similarly, for Pr_6O_{11} sample (Fig. 6c), the presence of $3d_{3/2}$ and $3d_{5/2}$ spin orbitals at 934 and 950 eV represent the Pr^{4+} oxidation state and the shoulder peaks at 929 and 955 eV represent Pr^{3+} oxidation state. Corresponding binding energy confirms the existence of Pr_6O_{11} in different oxidation state as $Pr^{3+/4+}$ [41]. From Fig. 6d, the XPS plot of Mn_3O_4 sample confirms the multiple Mn oxidation states (Mn^{2+}, Mn^{3+} and Mn^{4+}). The $2p_{1/2}$ and $2p_{3/2}$ peaks at 652 and 640 eV corresponds Mn^{3+}, and the shoulder peaks at 650 and 639 eV corresponds to Mn^{4+} and Mn^{2+} [42]. From the XPS data, we can confirm that the selected metal oxides exist in multiple oxidation states. The ratio of ($Ce^{3+}/Ce^{3+} + Ce^{4+}$), ($Pr^{3+}/Pr^{3+} + Pr^{4+}$), ($Sn^{2+}/Sn^{2+} + Sn^{4+}$) and ($Mn^{3+}/Mn^{4+} + Mn^{3+} + Mn^{2+}$) indicate the reducibility of the redox sample, and it is calculated from the XPS plots by integrated areas under lower oxidation state to that of the total area of all the peaks. The area ratio (in percentage) for the redox samples (RM ≡ CeO_2, SnO_2, Pr_6O_{11} and Mn_3O_4) are given in Table 2. From this data, it is clearly evident that the Mn_3O_4 sample has a better degree of reducibility,

which in turn enhances the oxygen vacancy concentration [43] than compared to other redox samples and may result in better soot oxidation activity. H_2-TPR data collected from the literature [7, 27, 42, 44] for the current redox samples (see Table 2) also reveals that the Mn_3O_4 reduces at much lower temperature than compared to other samples and it is in concurrence with the reducibility data obtained from XPS analysis.

Further, for a better understanding of oxygen species that are in association with redox metal, O 1s XPS analysis of all the redox samples are obtained and compared with each other. By observing the O1s peak of CeO_2, SnO_2, Pr_6O_{11} and Mn_3O_4 samples from Fig. 7 it can be seen that all the samples have peaks corresponding to O_α (lattice oxygen), O_β (surface adsorbed oxygen) and O_γ (oxygen present due to hydroxyls, chemisorbed water and carbonates) respectively [41]. Table 2 depicts the corresponding binding energies. Consideration of binding energy values of different peaks leads to better comparative study. Lower the binding energy of O_β peak, easier the release of surface adsorbed oxygen and thus take part in reaction efficiently [41]. From the data of binding energy, it is evident that Pr_6O_{11} has the lowest surface oxygen binding energy and then Mn_3O_4, followed by CeO_2. SnO_2 has higher binding energy value which can drop their catalytic activity compared to other samples. Lower the binding energy of surface adsorbed oxygen, easier the catalytic reaction and thus enhance the soot oxidation. Thus, Pr_6O_{11} and Mn_3O_4 are expected to show better catalytic activity compared to CeO_2 and SnO_2.

From XPS data, it is clearly evident that the Mn_3O_4 sample has higher reducibility than compared to other redox samples (Pr_6O_{11}, CeO_2 and SnO_2) and it may aid in soot oxidation activity since higher reducibility directly leads higher oxygen buffering capability [46]. From Table 2 it can be noticed that the Δr (ionic size difference of the corresponding metal oxide oxidation states) is small for the
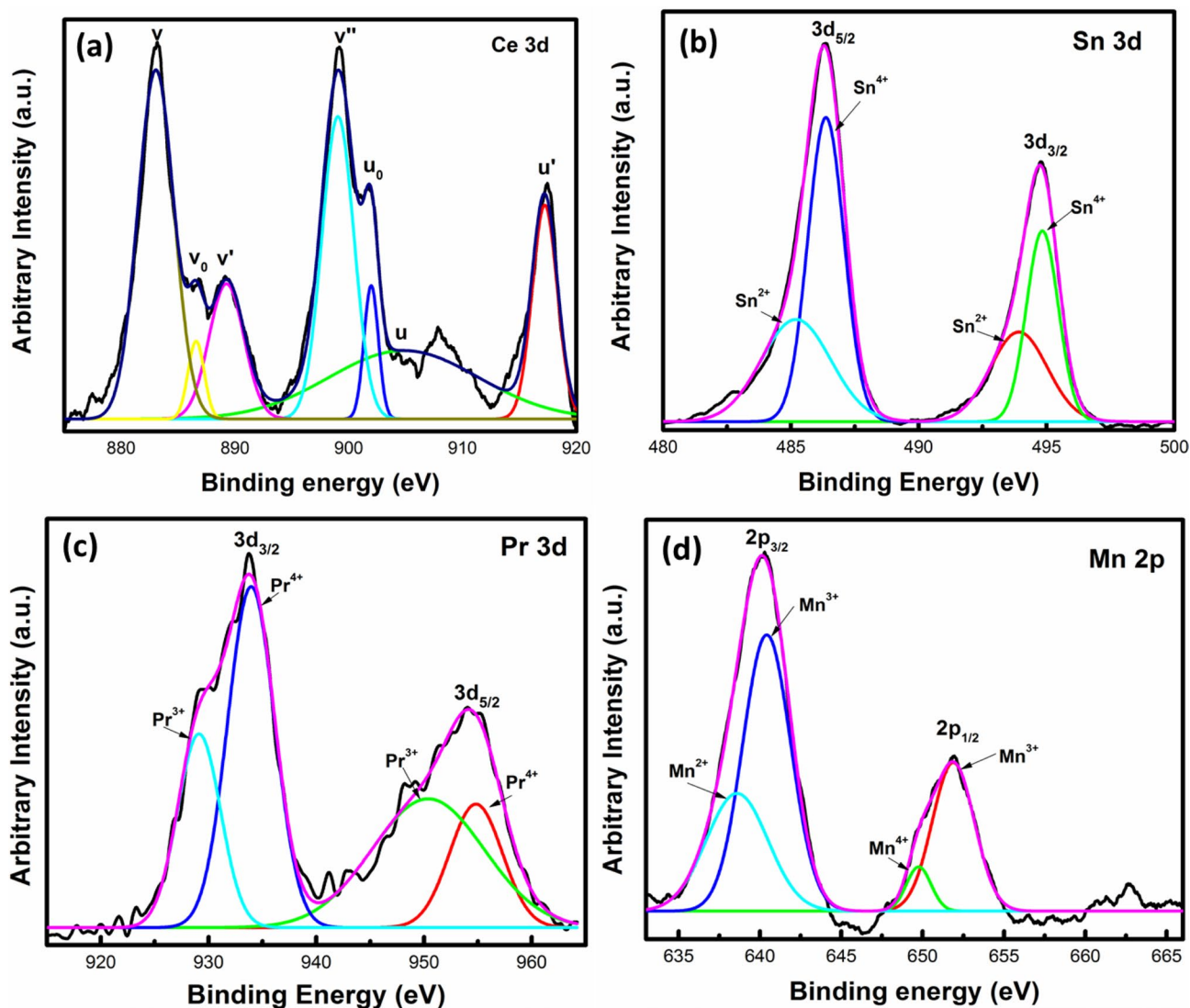
Fig. 6 XPS of **a** Ce 3d, **b** Sn 3d, **c** Pr 3d and **d** Mn 2p of the corresponding redox metal oxides

Mn_3O_4 sample followed by Pr_6O_{11} sample than compared to other redox samples (CeO_2 and SnO_2). From H_2-TPR studies obtained from literature [7, 27, 42, 44], the reduction temperatures [T_α (surface metal reduction) and T_β (bulk metal reduction)] are much lower for the Mn_3O_4 sample followed by the Pr_6O_{11} sample than compared to the other redox samples (CeO_2 and SnO_2). From the viewpoint of easy reducibility, lower reduction temperature and smaller Δr value, Mn_3O_4 and Pr_6O_{11} samples may lead to better soot oxidation activity than compared to CeO_2 and SnO_2 samples.

3.4.2 Non-Redox Metal Oxides

Figure 8 demonstrates the core level spectrum of Gd 4d, La 3d, Zr 3d and Hf 4f of the non-redox samples (Gd_2O_3, La_2O_3, ZrO_2 and HfO_2) and the corresponding O 1s peaks are depicted in Fig. 9. For Gd_2O_3 sample, the spin orbital doublet of $4d_{5/2}$ and $4d_{3/2}$ at 141.4 and 146.7 eV, respectively confirms the presence of Gd^{3+} oxidation state [47]. For La_2O_3 sample, La $3d_{5/2}$ dislayed multiple peaks at 834.9 and 838.4 eV with a 3.5 eV binding energy split. From litrature [41], the binding energy split for the same is ~4.0 eV and this confirms the presence of impurity phase and is identified as $La_2O_2CO_3$ from XRD data. For ZrO_2 and HfO_2 samples, the peaks at 181.5 eV (Zr $3d_{5/2}$) and 183.9 eV (Zr $3d_{3/2}$) confirms the presence of Zr^{4+} oxidation state and the peaks at 16.8 eV (Hf $4f_{5/2}$) and 18.6 eV (Hf $4f_{7/2}$) confirms the presence of Hf^{4+} oxidation state, respectively [41]. From the XPS results of non-redox metal oxides, it is evident that all these metal oxides exists only single oxidation state.

From Fig. 9, the relative percentage of surface oxygen (O_β) to the total oxygen ($O_\alpha + O_\beta + O_\gamma$) is calculated and shown in
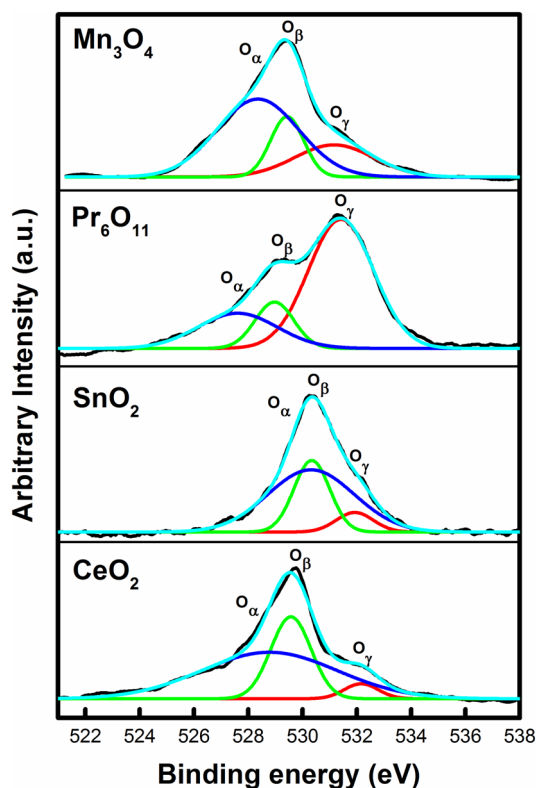
Fig. 7 O 1s XPS of CeO$_2$, SnO$_2$, Pr$_6$O$_{11}$ and Mn$_3$O$_4$ redox samples

Table 3. The decreasing order of relative surface oxygen to the total oxygen is in the order: HfO$_2$ (58%) > La$_2$O$_3$ (53%) > ZrO$_2$ (8%) > Gd$_2$O$_3$ (4%). This may play a vital role in soot oxidation activity and will be discussed later.
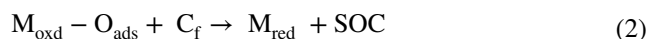
3.5 Soot Oxidation Activity

3.5.1 Redox Metal Oxides Soot Oxidation Activity

According to the soot oxidation mechanism proposed by Shangguan et al. [48] the metal oxide catalysts participate in a redox cycle, in which the metal repetitively gets oxidised and reduced. This mechanism is valid for many metal and metal oxide type catalysts [48, 49]. The following steps are involved in this mechanism [41]

$$M_{red} + O_{gas} \rightarrow M_{oxd} - O_{ads} \tag{1}$$

$$M_{oxd} - O_{ads} + C_f \rightarrow M_{red} + SOC \tag{2}$$

$$SOC \rightarrow CO/CO_2 \tag{3}$$

where M_{red} and $M_{oxd} - O_{ads}$ represent the reduced and oxidised states of the catalyst, respectively. O_{gas} and O_{ads} represent the gaseous O_2 and surface adsorbed oxygen species, respectively. C_f denotes the surface active site of carbon or free site on carbon surface, and SOC accounts for a surface carbon–oxygen complex. According to this mechanism, the gaseous oxygen is dissociatively adsorbed on the surface of the metal oxide catalyst and the resulting atomic O_{ads} species then attack the reactive free carbon site to give an oxygen-containing active intermediate. The reaction between the intermediate and either O_{ads} or the gaseous oxygen produces CO/CO_2 [48].

Figure 10 demonstrates the soot oxidation activity of the redox metal oxides. T_{50} temperature (temperature at which at least 50% of soot conversion takes place) is used as a reference point to evaluate the performance of catalysts. Mn$_3$O$_4$ and Pr$_6$O$_{11}$ catalysts showed much better soot oxidation activity followed by CeO$_2$ and SnO$_2$ catalysts when compared to bare soot oxidation activity. The observed T_{50} temperatures for the redox catalysts, Mn$_3$O$_4$, Pr$_6$O$_{11}$, CeO$_2$, and SnO$_2$ are 483, 485, 530 and 576 °C, respectively (see Table 2) indicating that the soot oxidation activity order is: Mn$_3$O$_4$ > Pr$_6$O$_{11}$ > CeO$_2$ > SnO$_2$. From the proposed mechanism of soot oxidation, it implies that the formation of the metal-oxide bond ($M_{oxd} - O_{ads}$) plays a critical role indicating that the active presence of surface adsorbed oxygen (O_β) in the metal oxides [11]. From the O 1s XP spectra, we can see that Mn$_3$O$_4$ and Pr$_6$O$_{11}$ samples have lowest binding energy value than compared to other samples. From the XPS analysis, it is also worthwhile to mention that the Mn$_3$O$_4$ sample has higher reducibility than compared to other samples indicating that the sample can readily undergo reduction (M_{red} + SOC). Apart from this, the Δr is smallest for Mn$_3$O$_4$ sample than compared to other samples. However, at this point, the role of Δr in soot oxidation is not clearly understood, and this matter of fact can be explored in our further investigations. In general, the soot oxidation reaction on manganese oxides is anticipated to occur through a Mars-van-Krevelen (MvK) reaction mechanism. This mechanism highlights the role of structural defects and the significance of lattice oxygen mobility. In this mechanism, the formed
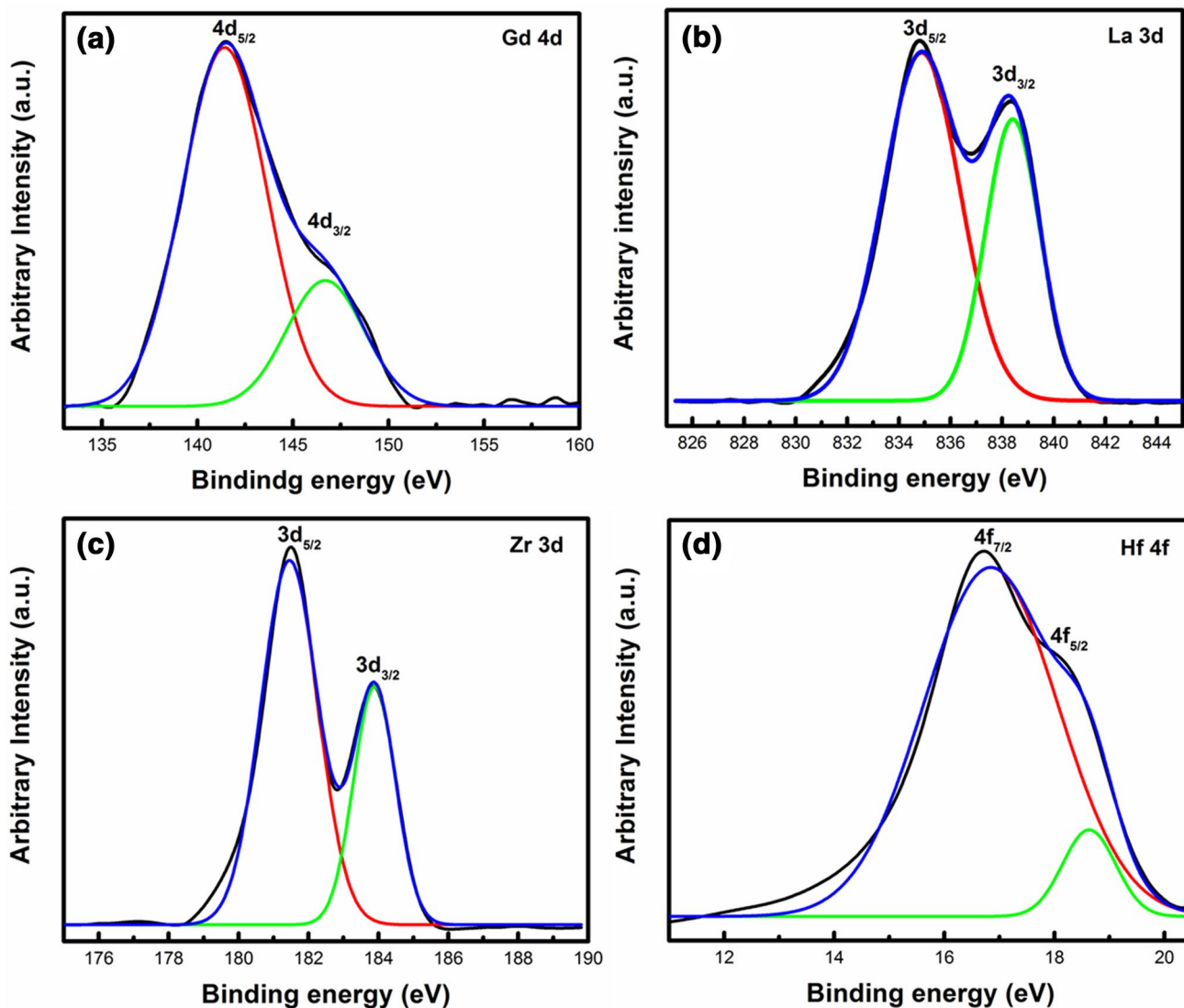
Table 2 Binding energy, reducibility ratio, H$_2$-TPR (T$_\alpha$/T$_\beta$), Δr and T$_{50}$ of redox metal oxides

Metal oxide	Binding energy (eV)			Reducibility ratio (%)	H$_2$-TPR (T$_\alpha$/T$_\beta$) (°C)	Δr (pm) [45]	T$_{50}$ (°C)
	O$_\alpha$	O$_\beta$	O$_\gamma$				
CeO$_2$	528.8	529.6	532.2	30	500/750 [44]	17	530
SnO$_2$	530.3	530.3	531.9	42	550/800 [7]	37	576
Pr$_6$O$_{11}$	527.6	528.9	531.4	33	512/550 [27]	17	482
Mn$_3$O$_4$	528.4	529.4	531.2	70	317/350 [42]	9 and 5	484

Fig. 8 XPS of **a** Gd 4d, **b** La 3d, **c** Zr 3d and **d** Hf 4f of the corresponding non-redox metal oxides

SOCs are oxidized at the soot-catalyst interface via reacting with lattice oxygen Eq. (4). The interaction is facilitated by catalyst reduction by transfer of oxygen from the bulk to its surface [50, 51].

$$C(O) + 2O^{2-} \text{ (lattice/surface)} + RM^{4+} \rightarrow CO_2 + RM^{3+} \tag{4}$$
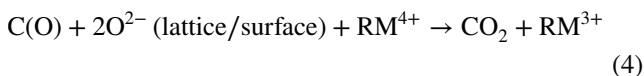
RM is redox metal (Ce, Sn, Pr and Mn).

For RM ≡ Ce, Sn and Pr the oxidation of SOCs at the soot-catalyst interface via reacting with surface adsorbed oxygen will be occurred through one step, Eq. (4) only. Whereas, for RM = Mn, the Mn^{3+} can be further reduced to Mn^{2+} due to its multiple step reduction behaviour which facilitates further the SOCs to react with lattice/surface oxygen ions (Eq. 5) and enhance the overall soot oxidation reaction.

$$C(O) + 2O^{2-} \text{ (lattice/surface)} + RM^{3+} \rightarrow CO_2 + RM^{2+} \tag{5}$$
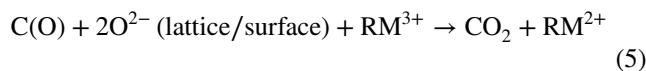
From this it is evident that the multiple redox steps ($Mn^{4+} \rightarrow Mn^{3+} \rightarrow Mn^{2+}$) can further enhance the soot oxidation activity than compared to single redox step ($RM^{4+} \rightarrow RM^{3+}$, RM ≡ Ce, Sn and Pr). From the present results it can infer that, for redox catalysts, the presence of surface adsorbed oxygen at lower binding energies, higher reducibility and smaller Δr govern the soot oxidation activity rather than the large surface area, greater pore volume and larger crystallite size.
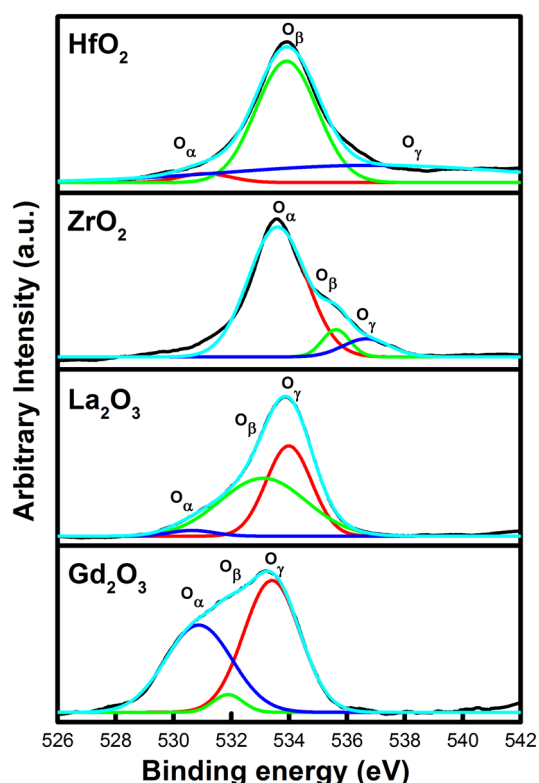
Fig. 9 O 1s XPS of Gd_2O_3, La_2O_3, ZrO_2 and HfO_2 non-redox samples

3.5.2 Non-Redox Metal Oxides Soot Oxidation Activity

Figure 11 illustrates the soot oxidation activity of non-redox metal oxides. The figure indicates that HfO_2 and ZrO_2 showed much better soot oxidation activity than La_2O_3 and Gd_2O_3. The T_{50} temperatures are 483, 494, 505 and 533 °C for HfO_2, ZrO_2, La_2O_3 and Gd_2O_3 respectively, indicating the soot oxidation activity order is $HfO_2 > ZrO_2 > La_2O_3 > Gd_2O_3$. Table 3 manifests that the increase in BET surface area, lattice strain and decrease in ionic radius follows the order: $HfO_2 > ZrO_2 > Gd_2O_3 > La_2O_3$. The relative percentage of surface oxygen to total oxygen $[O_\beta/(O_\alpha + O_\beta + O_\gamma)]$ obtained from XPS analysis followed same trend as soot oxidation activity apart from La_2O_3 sample. In general, smaller ionic radius of the cation enhances lattice oxygen mobility [5],

higher lattice strain increases the mobility of lattice oxygen and thus helps in oxygen migration [41, 52], and larger surface area leads to more number of active sites for soot oxidation and thus, enhance the soot oxidation activity [33]. The order of T_{50} temperature for soot oxidation activity follows the order of surface oxygen vacancy, surface area, lattice strain and ionic radius expect for La_2O_3 sample. This variation can be because of the presence of impurity ($La_2O_2CO_3$) in La_2O_3 sample which enhances the soot oxidation activity by carbon-intermediated mechanism [53]. Thus, in the case of non-redox samples other than La_2O_3 sample, surface features may aid in catalytic activity which benefits in surface oxygen that can be availed for soot oxidation reaction by spill over mechanism [51].

It is note worth to mention that the Gd_2O_3 sample showed the highest pore volume (0.0552 cm^3/g) (see Table 1) than compared to other samples which might help in better interaction between Gd_2O_3 sample and the soot particles in direct contact which enhances the transfer of the surface oxygens on the soot surface at catalyst interface, once transferred, gas phase oxygen fills the resulting vacancies and thus enhance the light-off (T_{10}) performance.

In case of non-redox metal oxides (Gd_2O_3, La_2O_3, ZrO_2 and HfO_2) surface oxygen has a key role since the reaction takes place when transfer of surface oxygen at soot-catalyst interface with the soot surface by spill over mechanism and form SOCs. This kind of surface mechanism is mainly aided through higher surface area, lattice strain and smaller ionic radius rather than multiple oxidation state of host cations. As a result of this study, further research will be focussing on binary and trinary metal oxides based on CeO_2 along with other oxides (HfO_2, Mn_3O_4 and Pr_6O_{11}) that showed better activity in the present work as a catalyst for soot oxidation reaction.

4 Conclusions

FTIR studies confirm the metal-oxide bond formation of all the metal oxides. XRD analysis revealed crystalline phase, size, lattice constant and lattice strain of metal oxides. For redox and non-redox metal oxides, smaller crystallite size, higher lattice strain, higher BET surface area is observed

Table 3 Binding energy, $O_\beta/(O_\alpha + O_\beta + O_\gamma)$, BET surface area, lattice strain, ionic radius and T_{50} of non-redox metal oxides

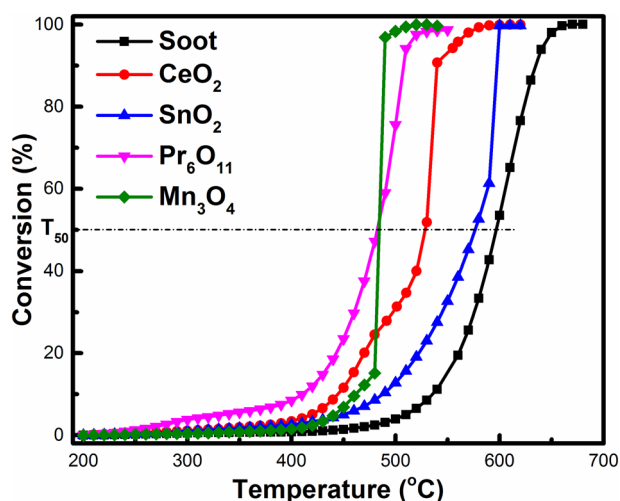| Metal oxide	Binding energy (eV)			$O_\beta/(O_\alpha + O_\beta + O_\gamma)$ (%)	BET Surface area (m^2/g)	Lattice strain (ε)	Ionic radii (pm)	T_{50} (°C)
	O_α	O_β	O_γ					
Gd_2O_3	530.9	531.9	533.4	4	4.6	0.0092	102.4	533
La_2O_3	530.6	533.1	533.9	53	0.9	0.0054	118.9	505
ZrO_2	533.6	535.6	536.7	8	7.2	0.0112	74.7	494
HfO_2	531.1	533.9	536.9	58	21.1	0.0157	58.2	483

Fig. 10 Soot oxidation of redox metal oxides (CeO_2, SnO_2, Pr_6O_{11} and Mn_3O_4)
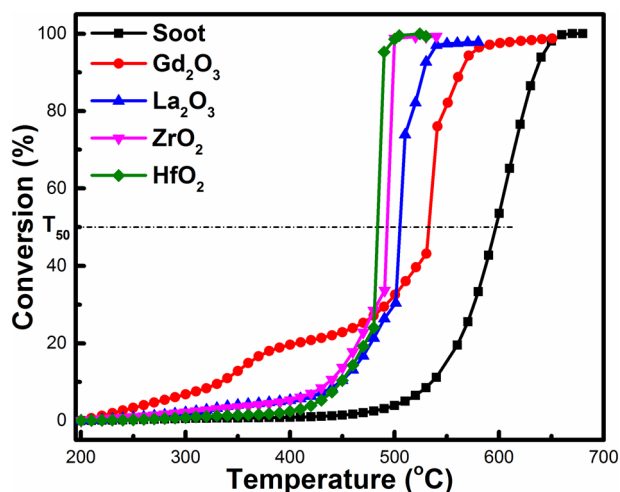

Fig. 11 Soot oxidation of non-redox materials (Gd_2O_3, La_2O_3, ZrO_2 and HfO_2)

for CeO_2 (11.7 nm, 0.0125 strain, 41.23 m^2/g) and HfO_2 (9.4 nm, 0.0157, 21.06 m^2/g), respectively. Among the redox metal oxide samples (CeO_2, SnO_2, Pr_6O_{11}, and Mn_3O_4), Mn_3O_4 and Pr_6O_{11} samples showed a better soot oxidation activity ($T_{50} = 484$ and 482 °C respectively). In redox metal oxides, lower binding energies, higher reducibility and smaller Δr govern the soot oxidation activity rather than the large surface area, greater pore volume and larger crystallite size. Among the non-redox metal oxides (Gd_2O_3, La_2O_3 ZrO_2 and HfO_2), HfO_2 sample displayed better soot oxidation activity ($T_{50} = 483$ °C). In non-redox metal oxides, higher surface oxygen, higher BET surface area, greater lattice strain and smaller ionic radius control the soot oxidation activity.

References

1. Wagloehner S, Nitzer-Noski M, Kureti S (2015) Chem Eng J 259:492
2. Campbell CT, Peden CHF (2005) Science 309:713
3. Neri G, Rizzo G, Galvagno S et al (2002) Thermochim Acta 381:165
4. Aneggi E, Boaro M, Leitenburg C de et al (2006) J Alloys Compd 408–412:1096
5. Rao GR, Mishra BG (2003) Bull Catal Soc India 2:122
6. Trovarelli A, Boaro M, Rocchini E et al (2001) J Alloys Compd 323–324:584
7. Ayastuy JL, Iglesias-González A, Gutiérrez-Ortiz MA (2014) Chem Eng J 244:372
8. Devaiah D, Tsuzuki T, Boningari T et al (2015) RSC Adv 5:30275
9. Thrimurthulu G, Komateedi, Rao N, Devaiah D, Benjaram, Reddy M (2012) Res Chem Intermed 38:1847
10. Atribak I, Bueno-López A, García-García A et al (2010) Appl Catal B 93:267
11. Christensen JM, Grunwaldt JD, Jensen AD (2016) Appl Catal B 188:235
12. Krishna K, Bueno-lópez A, Makkee M, Moulijn JA (2007) Appl Catal B 75:189
13. Neeft JPA, Makkee M, Moulijn JA (1996) Chem Eng J 64:295
14. Piumetti M, Bensaid S, Fino D, Russo N (2016) Appl Catal B 197:35
15. Vinodkumar T, Rao BG, Reddy BM (2015) Catal Today 253:57
16. Sunstrom JE, Ramanujachary KV, Greenblatt M, Croft M (1998) J Solid State Chem 139:388
17. Anil PS, Nair SPN, Alias JP, Date SK (1998) J Mater Chem 8:2245
18. Dasari HP, Ahn JS, Ahn K et al (2014) Solid State Ionics 263:103
19. Liu Y-F, Liu X-Q, Meng G-Y (2001) Mater Lett 48:176
20. Prasad DH, Park SY, Oh E-O et al (2012) Appl Catal A 447–448:100
21. Mcdevitt NT, Baun WL (1964) Spectrochim Acta 20:799
22. Want B, Dar F (2012) J Cryst Process Technol 2:137
23. Saravani H, Jehali M (2016) Orient J Chem 21:491
24. Damyanova S, Pawelec B, Arishtirova K et al (2008) Appl Catal A 337:86
25. Atribak I, Bueno-López A, García-García A (2008) Catal Commun 9:250
26. Chen W, Ghosh D, Chen S (2008) J Mater Sci 43:5291
27. Du Y, Zhu X, Wang H et al (2015) J Energy Inst 89:1
28. Khan SA, Gambhir S, Ahmad A (2014) Beilstein J Nanotechnol 5:249
29. Ghiasi M, Malekzadeh A (2015) Superlattices Microstruct 77:295
30. Keramidas VG, White WB (1974) J Am Ceram Soc 57:2

31. Ho M-Y, Gong H, Wilk GD et al (2003) J Appl Phys 93:1477
32. Li D, Meng F, Yan X et al (2013) Nanoscale Res Lett 8:1
33. Liang Q, Wu AX, Xiaodi A et al (2007) Catal Lett 119:265
34. Aneggi E, de Leitenburg C, Llorca J, Trovarelli A (2012) Catal Today 197:119
35. Shen Y, Chen Z, Zhou T et al (2016) J Mater Chem C 4:254
36. Zhou Z, Tian N, Li J et al (2011) Chem Soc Rev 40:4167
37. Chellappan L, Sanjeeviraja C (2014) J Adv Ceram 3:171
38. Nezhad EH, Ghorbani M, Zeinalkhani M, Heidari A (2013) Am J Chem 3:6
39. Chudobova D, Nejdl L, Gumulec J et al (2013) Int J Mol Sci 14:13592
40. Kumar E, Selvarajan P, Muthuraj D (2013) Mater Res 16:269
41. Mukherjee D, Rao BG, Reddy BM (2016) Appl Catal B 197:105
42. Zhan S, Zhu D, Qiu M et al (2015) RSC Adv 5:29353
43. Venkataswamy P, Jampaiah D, Mukherjee D et al (2016) Catal Lett 146:2105
44. Zhang W, Niu X, Chen L et al (2016) Nature 6:29062
45. Shannon RD (1976) Acta Mater A32:751
46. Trovarelli A (1999) Comments Inorg Chem 20:263
47. Durgasri DN, Vinodkumar T, Sudarsanam P, Reddy BM (2014) Catal Letters 144:971
48. Shangguan WF, Teraoka Y, Kagawa S (1997) Appl Catal B 12:237
49. Aneggi E, Leitenburg C, De Dolcetti G, Trovarelli A (2006) Catal Today 114:40
50. Wasalathanthri ND, SantaMaria TM, Kriz DA et al (2017) Appl Catal B 201:543
51. Mul G, Kapteijn F, Doornkamp C, Moulijn JA (1998) J Catal 179:258
52. Rushton MJD, Chroneos A, Skinner SJ et al (2013) Solid State Ionics 230:37
53. Aneggi E, De Leitenburg C, Dolcetti G, Trovarelli A (2007) Top Catal 42–43:319